Energy Storage Materials xxx (xxxx) xxx–xxx

Contents lists available at ScienceDirect

Energy Storage Materials

journal homepage: www.elsevier.com/locate/ensm

Stable three-dimensional metal hydride anodes for solid-state lithium storage

Fangjie Mo[a,1], Xiaowei Chi[b,1], Sangpu Yang[a], Feilong Wu[a], Yun Song[a], Dalin Sun[a], Yan Yao[b,*], Fang Fang[a,*]

[a] Department of Materials Science, Fudan University, Shanghai 200433, China
[b] Department of Electrical and Computer Engineering and TcSUH, University of Houston, Houston, TX 77204, USA

ARTICLE INFO

Keywords:
Alanate
Lithium ion battery
Hierarchical structure
Solid electrolyte

ABSTRACT

Since the discovery of metal hydrides as a conversion-type anode in lithium-ion batteries in 2008, many metal hydrides have been investigated for lithium-ion battery anodes. Although much progress has been made, metal hydrides still face severe challenges such as poor first cycle reversibility, low electrical conductivity, and high reactivity with liquid electrolyte. Here we demonstrate a three-dimensional hierarchical metal hydride/graphene composite ($LiNa_2AlH_6$/3DG) that shows the best performance among reported metal hydride anodes. $LiNa_2AlH_6$ nanoparticles are uniformly anchored on graphene nanosheets which self-assemble into the 3D microflowers hierarchical structure, and exhibit outstanding cycling stability with $LiBH_4$ as a solid electrolyte. An ultra-high capacity of 861 mA h g^{-1} at the current density of 5 A g^{-1} and a long cycle life of 500 cycles with capacity retention of 97% are demonstrated. These findings pave the way for designing nanoscale metal hydrides as electrode materials in solid-state lithium batteries.

1. Introduction

High-energy lithium-ion batteries for electrical energy storage have transformed our lifestyle with tremendous impact to the modern society. Graphite is used as the commercial anode material based on intercalation reaction; however, graphite has the low theoretical capacity (372 mA h g^{-1}) and unsafe Li^+ intercalation voltage (~0.2 V) due to potential lithium plating during battery fast charging. Searching for novel anode materials with enhanced Li storage capacity and suitable working voltage has never stopped [1–3]. Alternative battery anode materials could utilize conversion reactions. Metal oxides, sulfides, nitrides, phosphides, and fluorides show high theoretical capacity due to two or more electrons per redox center [4–8]. In 2008, Aymard et al. reported the first metal hydride as a conversion-type anode material with a surprisingly small polarization between the charge-discharge curves [9]. The difference of polarization behaviour compared to those of oxides and fluorides can be understood on the basis of ionocovalency of metal-X bond (X = O, S, N, P, F or H) [9,10].

Since this discovery in 2008, many metal hydrides have been investigated for lithium-ion battery anodes [9–21]. In particular, alanate compounds, such as $LiAlH_4$ [22,23], $NaAlH_4$ [23–29], Na_3AlH_6 [24,25], $LiNa_2AlH_6$ [25], show high theoretical capacity (1576–2680 mA h g^{-1}) and low working potential (0.1–1 V *vs.* Li^+/Li). Table S1 summarizes the performance of alanates from the literatures. Although much progress has been made, alanates still face severe challenges. The first challenge is low reversibility in the first cycle [24]. For example, $LiAlH_4$ delivered initial discharge and charge capacities of 1180 and 188 mA h g^{-1}, respectively, leading to a low coulombic efficiency of 10% [22]. Second, the intrinsic electrical conductivity of alanates is very low, similar to most metal hydrides, therefore an electrical conductive matrix is needed to enhance its electronic transport [30–33]. Forming an intimate contact between conductive carbon and alanates is non-trivial due to the difficulty of using liquid phase or solution phase mixing methods for alanates [34,35]. The third challenge is the agglomeration of discharged products that reduces active sites and cycling reversibility [36]. Finally, the high reactivity of H^- in the alanates could lead to undesired side reactions with electrolytes. Real et al. showed that spontaneous chemical decomposition of $LiPF_6$-based liquid electrolyte starts as soon as the electrolyte is in contact with $NaAlH_4$ [29].

To counter these challenges, we decide to select a suitable metal hydride with intrinsic reversibility. So far there is no established principle guiding the selection of metal hydride as a battery anode. From the conversion reaction of alanates ($M_xAl_yH_z + ne^- + nLi^+ \rightarrow xM^0 + yAl^0 + zLi_mH$ ($m = n/z$)), it can be found that during electrochemical

* Corresponding authors.
E-mail addresses: yyao4@uh.edu (Y. Yao), f_fang@fudan.edu.cn (F. Fang).
[1] F. Mo and X. Chi contributed equally to this work.

https://doi.org/10.1016/j.ensm.2019.01.014
Received 12 October 2018; Received in revised form 22 January 2019; Accepted 22 January 2019

discharge, H anions desorb from alanates and combine with Li^+ to form LiH, corresponding to the dehydrogenation of alanates; during the charge, H anions desorb from LiH and hydrogenate Al and M. Since the dehydrogenation and hydrogenation of alanates are used to evaluate the hydrogen storage reversibility when alanates are studied as hydrogen storage materials, the reversibility of alanates as a battery anode has an intrinsic connection with the reversibility of its hydrogen storage. The established knowledge in hydrogen storage teaches us that a moderate reaction enthalpy (ΔH) is beneficial for reversible dehydrogenation and hydrogenation. When ΔH is too large, dehydrogenation is difficult; when ΔH is too small, rehydrogenation becomes unfavorable. Due to the similarity between chemical reactions in hydrogen storage and electrochemical reactions in lithium-ion batteries, we hypothesize that ΔH may also play an important role in anode selection. Table S2 lists the reaction enthalpy of various alanates as well as the temperature and pressure corresponding to dehydrogenation and hydrogenation reactions for each compound. $LiNa_2AlH_6$ stands out as the most reversible hydrogen storage analates with an optimal ΔH value of 53.0 kJ mol^{-1}, therefore we select $LiNa_2AlH_6$ as a model compound in this study.

In this work, we demonstrate a two-step method in the synthesis of three-dimensional hierarchical $LiNa_2AlH_6$/graphene composites ($LiNa_2AlH_6$/3DG), where nanosized $LiNa_2AlH_6$ is uniformly anchored in the hierarchical graphene network. Two electrolytes, $LiPF_6$-based carbonate liquid electrolyte, and $LiBH_4$ solid electrolyte were applied to investigate the cell performance of the $LiNa_2AlH_6$/3DG anode. In contrast to a continuous capacity loss in the liquid electrolyte, far better cycling stability and superior rate performance have been demonstrated for $LiNa_2AlH_6$/3DG using the solid electrolyte.

2. Experimental section

2.1. Synthesis of $LiNa_2AlH_6$/3DG composites

Na (95% purity), NaH (95% purity), $LiAlH_4$ (95% purity), $LiBH_4$ (95% purity), THF (ultra-pure dry, 99.9%), and Naphthalene ($C_{10}H_8$, 99%) were purchased from Sigma-Aldrich and used as received without further purification. Graphene (XFNANO) was treated at 600 °C under vacuum overnight to remove absorbed water and oxygen. $LiNa_2AlH_6$/3DG hierarchical composites were synthesized using a two-step method. In a typical synthesis, Na (114 mg) and $C_{10}H_8$ (667 mg) were dissolved in anhydrous THF (50 mL), and then graphene (71 mg) was added and continuously stirred for 1 h. The dispersion was then transferred to a reactor and heated at 90 °C under 3 MPa in H_2 atmosphere for 12 h with continuous magnetic stirring. An intermediate NaH/Graphene (NaH/G) composite was obtained by filtration, washing with anhydrous THF, and drying at 60 °C. Finally, NaH/G (200 mg) and $LiAlH_4$ (99 mg) were ball-milled in a planetary ball-milling machine at 400 rpm for 36 h under 4 MPa H_2 atmosphere, resulting in the $LiNa_2AlH_6$/3DG microflower composite. The ball-to-powder mass ratio is 40:1.

2.2. Material characterizations

XRD patterns were collected on a Bruker D8 Advance X-ray diffractometer with Cu Kα radiation (λ=1.5406 Å). Cycled battery electrodes were washed with anhydrous diethyl carbonate to remove the remaining electrolyte, and Scotch tape was used to protect samples from being contaminated by air or moisture during the XRD measurement. Morphology and structures of samples were investigated using FEI Nova Nano 450 field-emission scanning electron microscope and an FEI Tecnai G2 F20 S-Twin transmission electron microscope. FTIR spectra were recorded over 32 scans in transmission mode at a resolution of 4 cm^{-1} using a Nicolet iS50 FT-IR. Thermal decomposition behavior was measured using a Netzsch STA 409 PC at a heating rate of 5 °C min^{-1} under Ar atmosphere.

2.3. Liquid electrolyte batteries

To fabricate the cathode, $LiNa_2AlH_6$ and carbon additive (Super P) were ball-milled in a mass ratio of 7:3 at 250 rpm for 2 h under a hydrogen atmosphere of 1 MPa. 2 mg mixed powders were then uniformly spread onto a nickel foam current collector and pressed into a pellet under a pressure of 10 MPa. No polymer binder was used to avoid potential reaction with $LiNa_2AlH_6$. Coin-type half-cells (2032) were assembled using the pellet as the cathode, Li metal as the anode, porous polypropylene membrane as the separator, and 1 M $LiPF_6$ ethylene carbonate and dimethyl carbonate (1:1) as the electrolyte.

2.4. Solid state batteries

Battery assembly was carried out in an Ar-filled glove box with water and oxygen below 0.1 ppm. $LiNa_2AlH_6$/3DG, carbon additives (Timcal Super C65) and $LiBH_4$ powders (Sigma-Aldrich, ≥ 95%) were mixed in an agate mortar at a weight ratio of 3:3:4 for the cathode. To assemble a solid-state cell, 50 mg $LiBH_4$ was firstly pressed in the PEEK die (Φ = 13 mm) under 1 metric ton pressure. The mixed cathode powders (~2 mg) were then uniformly distributed on top of the solid-state electrolyte and pressed under a pressure of 4 metric tons into a bi-layer pellet. Li metal foil was attached to the other side of solid-state electrolyte as the anode. During the cell test, a constant pressure of 20 psi was applied.

2.5. Electrochemical measurement

Galvanostatic charge-discharge cycling was performed within a potential range of 0.01–1.0 V *vs.* Li^+/Li using a battery tester (CT2001A, LAND). Cyclic voltammetry (CV) and electrochemical impedance spectroscopy (EIS) were performed on a potentiostat (VMP3, Biologic LLC). During the test, the temperatures were maintained at 25 °C for liquid batteries and 125 °C for solid batteries. C-rate and specific capacities were calculated based on the mass of $LiNa_2AlH_6$.

3. Results and discussion

3.1. Hierarchical structure design and preparation

A two-step *in-situ* synthesis method as illustrated in Fig. 1 was developed to prepare $LiNa_2AlH_6$/3DG for improving electrical conductivity and avoiding agglomeration. First, an intermediate composite of NaH and graphene (NaH/G) was synthesized by one-step solvothermal reaction of sodium naphthalenide ($C_{10}H_8Na$) supported by graphene dispersed in tetrahydrofuran (THF) under a hydrogen pressure of 3 MPa. During the solvothermal reaction, NaH was formed *in-situ* supported by the XRD patterns in Fig. 2a. The TEM image of NaH/G and corresponding EDX mapping (Fig. 2b and c) confirmed that nanosized NaH was uniformly anchored on graphene surface. Second, NaH/G and $LiAlH_4$ were ball-milled with a molar ratio of 2:1. During the ball-milling, $LiAlH_4$ reacted with nanosized NaH to form $LiNa_2AlH_6$ which was anchored on graphene, meanwhile, graphene self-assembled into a morphology of 3D hierarchical microflower. Pure $LiNa_2AlH_6$ phase was found after ball-milling, revealing that NaH and $LiAlH_4$ have all been converted into $LiNa_2AlH_6$. Fourier-transform infrared spectra in Fig. S1 showed two broad and strong peaks at ~1420 cm^{-1} and ~813 cm^{-1}, assigned to the Al–H vibration mode in $LiNa_2AlH_6$. Moreover, the 3D hierarchical microflower morphology of $LiNa_2AlH_6$/3DG were clearly observed in the SEM and TEM images (Fig. 2d and e). The corresponding EDS elemental mapping of $LiNa_2AlH_6$/3DG (Fig. 2f) presented uniform distribution of Na, Al, and C, suggesting an intimate contact between $LiNa_2AlH_6$ and graphene. To determine the exact composition of $LiNa_2AlH_6$ in the composite, thermogravimetric analysis (Fig. S2) was performed and $LiNa_2AlH_6$/3DG desorbed about 4.07 wt% hydrogen, translating to 70 wt% $LiNa_2AlH_6$ in the $LiNa_2AlH_6$/3DG composite.

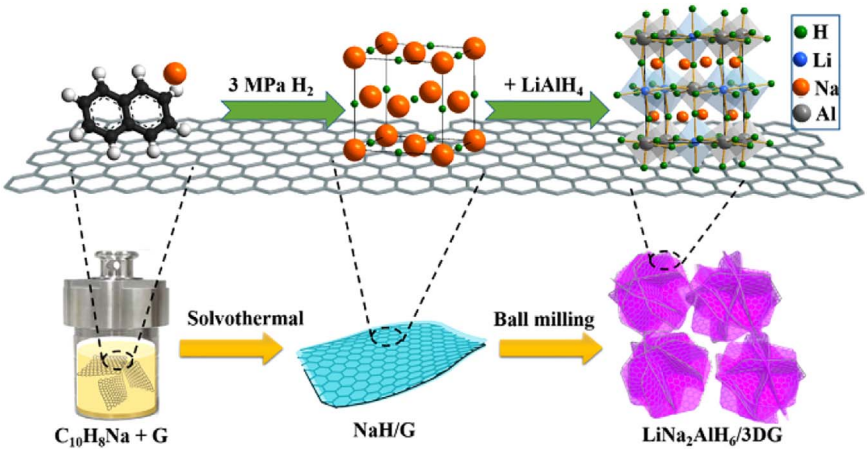

Fig. 1. Schematic illustration of synthesis procedures of $LiNa_2AlH_6$/3DG.

3.2. Improved cycling stability of $LiNa_2AlH_6$/3DG in $LiPF_6$-based liquid electrolyte

$LiNa_2AlH_6$ has been previously studied by Reale et al., in which the first cycle coloumbic efficiency was only about 34% and no cycling performance was reported [24]. $LiNa_2AlH_6$ has a large theoretical capacity of 1558 mA h g^{-1} based on following conversion reaction:

$$LiNa_2AlH_6 + 5e^- + 5Li^+ \rightarrow 2Na + Al + 6LiH$$

To understand the advantages of 3D hierarchical structure on electrochemical performance, we prepared a control sample by ball-milling $LiNa_2AlH_6$ and graphene (labeled as $LiNa_2AlH_6$+G). Fig. 3 presented the Li-storage performance of $LiNa_2AlH_6$/3DG and $LiNa_2AlH_6$+G with a cut-off voltage of 1 V at the current density of 0.1 A g^{-1}. As shown in Fig. 3a, a long discharge plateau at 0.25 V and a charge plateau at 0.8 V were observed for $LiNa_2AlH_6$/3DG and the initial discharge and charge capacities were 2396 and 1612 mA h g^{-1}, revealing a low initial coulombic efficiency of ca. 67%. This low coulombic efficiency was mainly attributed to the large irreversible capacity of graphene, a large discharge capacity of 2443 mA h g^{-1} but a small charge capacity of 234 mA h g^{-1} under the cut-off voltage of 1 V (Fig. S3a). In the second cycle, the coulombic efficiency of $LiNa_2AlH_6$/3DG in Fig. 3b increased to 90% and its discharge and charge capacities were ca. 1580 and 1420 mA h g^{-1}, respectively. With increasing cycling number, the charge capacity of $LiNa_2AlH_6$/3DG slowly decreased to 1020 mA h g^{-1}. For the control sample of $LiNa_2AlH_6$+G, the discharge-charge voltage profiles in the first few cycles were consistent with those of $LiNa_2AlH_6$/3DG. However, with increasing cycle number, $LiNa_2AlH_6$+G showed faster capacity decay than that of $LiNa_2AlH_6$/3DG. The charge capacity retention of $LiNa_2AlH_6$+G decreased to 21.3% after 100th cycle, which was only half of that of $LiNa_2AlH_6$/3DG. Table S1 summarizes the performance of this work with previously reported alanates anode. A notable improvement of cycling stability in $LiNa_2AlH_6$/3DG is due to its unique 3D hierarchical structure.

To study the charge product of the reaction, *ex-situ* XRD measurements of $LiNa_2AlH_6$/3DG at various states of discharge were performed to understand the structural evolution. The XRD patterns in Fig. 3f clearly show the peak at 34.2 degree corresponding to $LiNa_2AlH_6$ gradually decreases from A to E during the discharge and gradually increases from E to G during the charge, reflecting the excellent reversibility of $LiNa_2AlH_6$. Further evidence could be found from the linear scanning voltammetry (LSV) curves of pristine $NaAlH_4$,

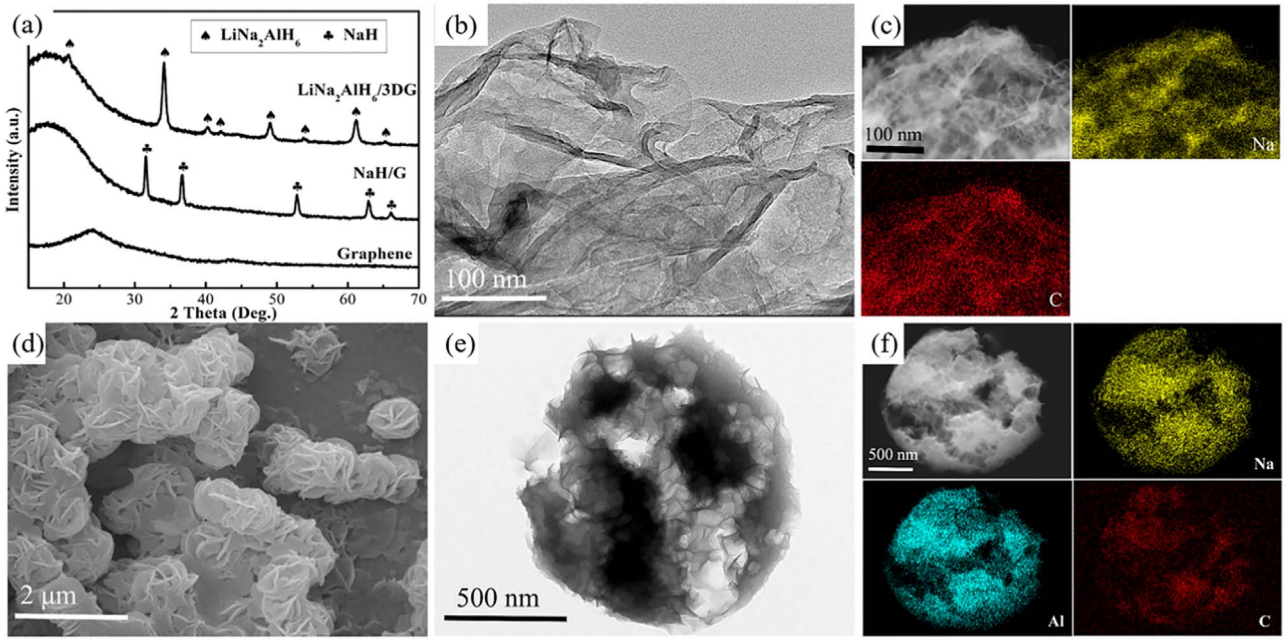

Fig. 2. (a) XRD patterns of graphene, NaH/G and $LiNa_2AlH_6$/3DG; (b) TEM images and (c) HAADF-STEM image and the corresponding Na and C mapping images of NaH/G; (d) SEM, (e) TEM images, and (f) HAADF-STEM image and corresponding Na, Al, C elemental mapping of the $LiNa_2AlH_6$/3DG.

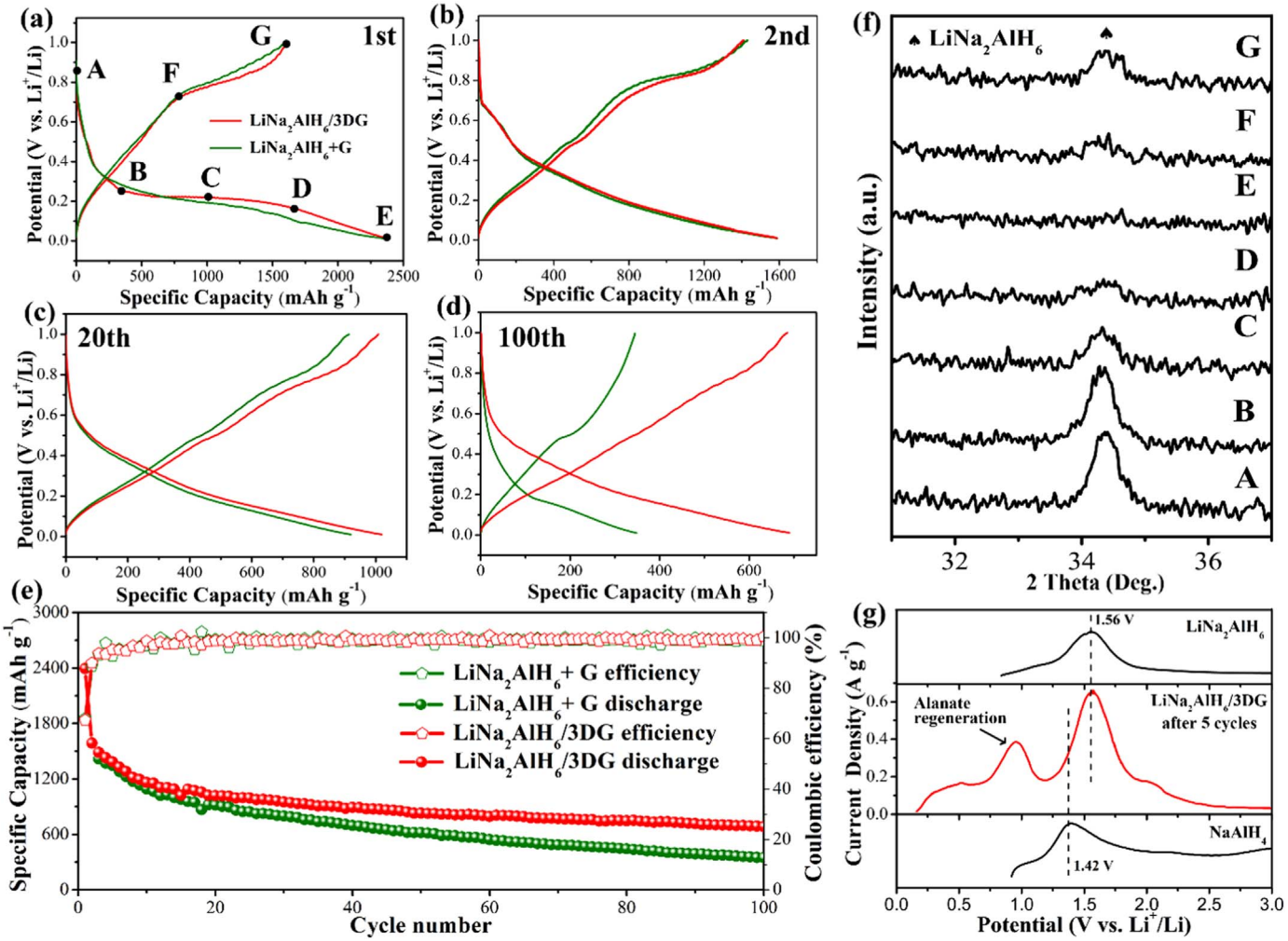

Fig. 3. Galvanostatic discharge-charge voltage profiles of $LiNa_2AlH_6$/3DG and $LiNa_2AlH_6$+G. (a) 1st, (b) 2nd, (c) 20th, and (d) 100th cycle. The voltage cut-off is 1 V vs. Li/Li^+ and current density is 0.1 A g^{-1}. (e) Cycle performance fr 100 cycles. (f) Ex-situ XRD patterns of the $LiNa_2AlH_6$/3DG electrode at different states of discharge. (g) Comparison of LSV of the pristine $NaAlH_4$, pristine $LiNa_2AlH_6$, and discharged product of $LiNa_2AlH_6$/3DG (the fifth cycle).

pristine $LiNa_2AlH_6$, and its discharged product displayed in Fig. 3g. $NaAlH_4$ was chosen as a reference sample since both $NaAlH_4$ and $LiNa_2AlH_6$ could be regenerated from the discharged composite of Na, Al and LiH but the former shows poor reversibility [28,29]. Both $NaAlH_4$ and $LiNa_2AlH_6$ show unique anodic decomposition peaks as 1.42 V and 1.56 V vs Li^+/Li, respectively. For the discharged products of $LiNa_2AlH_6$/3DG after 5 cycles, we observe the anodic peak at 1.56 V, indicating that $LiNa_2AlH_6$ rather than $NaAlH_4$ was regenerated and the regeneration of $LiNa_2AlH_6$ led to the improvement in cycling stability.

3.3. Excellent performance of $LiNa_2AlH_6$/3DG with $LiBH_4$ solid electrolyte

Although the cycling stability shown in Fig. 3e was improved compared to earlier reports, capacity decay still existed, mainly attributed to the side reactions between H^- anions in the regenerated $LiNa_2AlH_6$ and liquid electrolyte [22,28,29]. Kojima and Latroche et al. demonstrated that MgH_2 that has a similar H^- anion that can form a stable interface with hydride-based solid-state electrolyte, such as $LiBH_4$ or $LiBH_4$-LiI [34,37,38]. In this work we also investigated $LiBH_4$ as a solid-state electrolyte to further improve cycle stability of $LiNa_2AlH_6$/3DG. Fig. 4a shows the galvanostatic discharge–charge profiles for $LiNa_2AlH_6$/3DG with $LiBH_4$ electrolyte at 125 °C, at which $LiBH_4$ is a hexagonal phase with ionic conductivity of 1.8 mS/cm. The profiles of the first two discharge–charge curves were similar to those in the liquid electrolyte (Fig. 3a and b), indicating that $LiNa_2AlH_6$ was well regenerated. Furthermore, similar dQ/dV profiles of $LiNa_2AlH_6$/3DG in $LiBH_4$ electrolyte and $LiPF_6$-based liquid electrolyte were shown in Fig. S4, indicating similar electrochemical reaction mechanisms of $LiNa_2AlH_6$/3DG in the solid and liquid electrolytes. From Fig. 4a and b, the voltage profiles stabilized after a few cycles and led to a stable capacity at 1280 mA h g^{-1} for 50 cycles at 0.2 A g^{-1}. Fig. 4c shows a capacity retention of 97% for 500 cycles for $LiNa_2AlH_6$/3DG at the current density of 1 A g^{-1}, the best stability among alanates anodes to the best of our knowledge. Fig. 4d shows the rate capability of $LiNa_2AlH_6$/3DG and the discharge capacities of $LiNa_2AlH_6$/3DG are 1163, 1034, 979, 925 and 861 mA h g^{-1} at the current density of 0.2, 0.5, 1, 2 and 5 A g^{-1}, respectively. Fig. 4e shows the Nyquist plot of the electrochemical impedance spectrum of $LiNa_2AlH_6$/3DG. The semicircle representing the charge-transfer resistance in the high-frequency range is very small, indicating negligible interfacial resistance between $LiNa_2AlH_6$/3DG and $LiBH_4$ electrolyte, ensuring the high rate performance observed in Fig. 4d [35].

To shed light on the excellent cycling stability of $LiNa_2AlH_6$/3DG compared to other alanates, we summarize that the $LiNa_2AlH_6$/3DG composite has following three advantages. First, $LiNa_2AlH_6$ has better intrinsic reversibility. Compared to other hydrides shown in Table S2, $LiNa_2AlH_6$ decomposes at an onset temperature of 207 °C and can be rehydrogenated at 2.9 bar at 170 °C, indicating a superior reversibility under relatively mild conditions. The optimal ΔH value of $LiNa_2AlH_6$

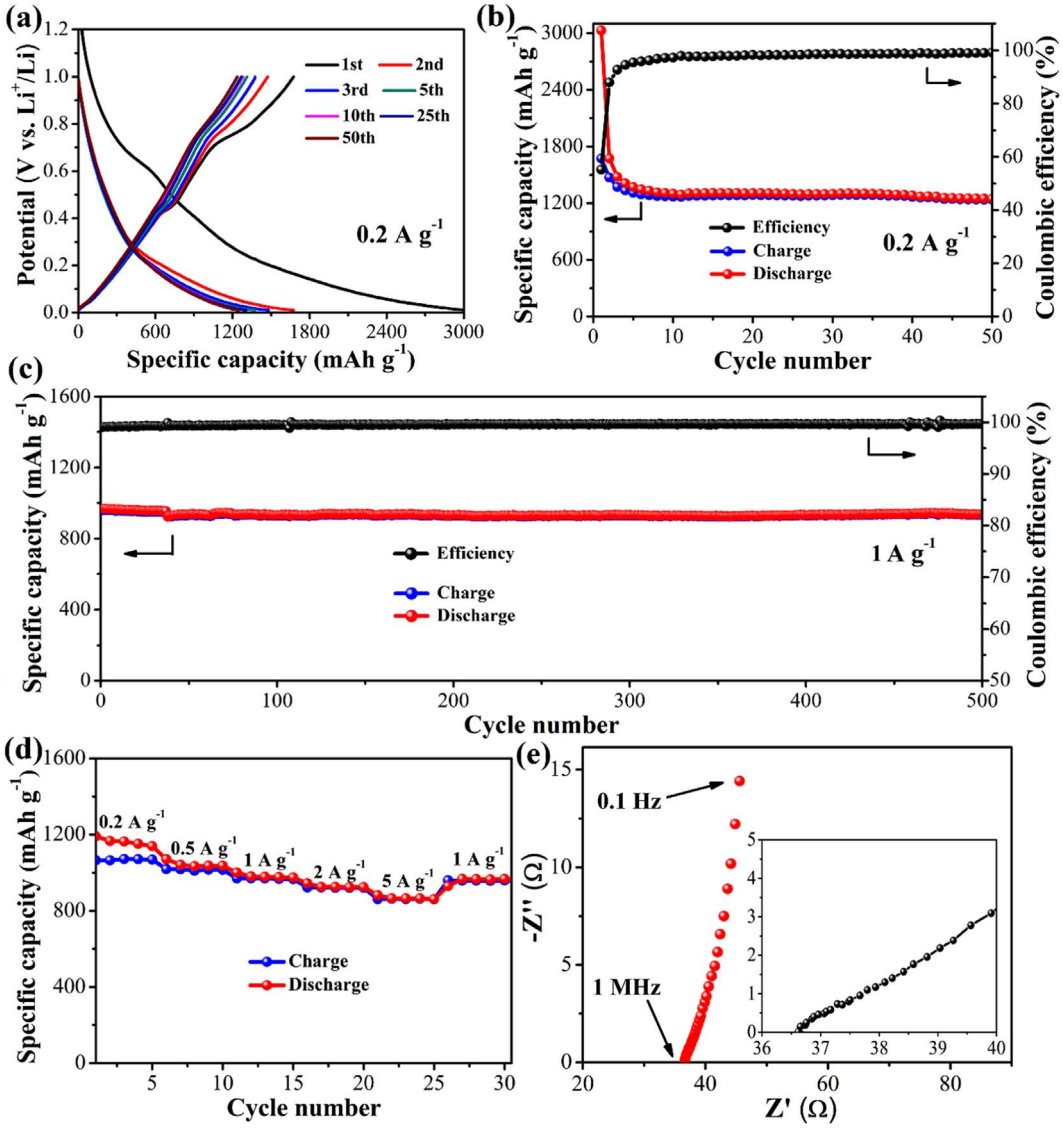

Fig. 4. Li-storage performance of $LiNa_2AlH_6$/3DG with $LiBH_4$ solid electrolyte at 125 °C: (a) discharge-charge voltage profiles at 0.2 A g^{-1}; the cycling performance at (b) 0.2 A g^{-1} and (c) 1 A g^{-1}, respectively; (d) the rate capability from 0.2 A g^{-1} to 5 A g^{-1}; (e) Nyquist plot of electrochemical impedance spectrum at the open circuit voltage.

forms the basis of reversible electrochemical cycling. Second, in the hierarchical structure of $LiNa_2AlH_6$/3DG, $LiNa_2AlH_6$ nanoparticles are uniformly and intimately anchored on graphene nanosheets which further self-assemble into 3D microflowers. Such a structure with three hierarchical levels (i.e. nanoparticles, nanosheets, and microflowers) not only provides rich active sites, high electrical conductivity and short Li^+ diffusion path but also inhibits the aggregation of active materials and stabilizes the hierarchical structure. Finally, ultrafast charge-transfer process and compatible interface between $LiNa_2AlH_6$ and $LiBH_4$ solid-state electrolyte further improve the Li-ion battery performance.

4. Conclusions

In summary, we report a two-step method for the $LiNa_2AlH_6$/graphene composite synthesis. $LiNa_2AlH_6$/3DG delivers a high capacity of 861 mA h g^{-1} at a high current density of 5 A g^{-1} and a stable cycle capacity for 500 cycles in an all-solid-state Li-ion battery with $LiBH_4$ solid-state electrolyte. The Li-storage performance of $LiNa_2AlH_6$/3DG in the solid-state battery is substantially better than previous reports of alanates anodes, which is attributed to the better intrinsic reversibility of $LiNa_2AlH_6$, the hierarchical structure of $LiNa_2AlH_6$/3DG, and the ultrafast charge-transfer process and stable interface between $LiNa_2AlH_6$/3DG and $LiBH_4$. This work not only demonstrates the improvement of hydrides anode performance but also guides the design of metal hydride anodes.

Acknowledgements

This work was financially supported by the National Natural Science Foundation of China (No. 51601040, 51471052, and 51571063) and the Science and Technology Commission of Shanghai Municipality (No. 15YF1401300).

Competing financial interests

The authors declare no competing financial interests.

Data availability

The raw data required to reproduce these findings are available from the corresponding authors. The processed data required to reproduce these findings are available from the corrresponding atuhors.

Appendix A. Supporting information

Supplementary data associated with this article can be found in the online version at doi:10.1016/j.ensm.2019.01.014.

References

[1] Y.X. Yin, S. Xin, Y.G. Guo, L.J. Wan, Lithium–sulfur batteries: electrochemistry, materials, and prospects, Angew. Chem. Int. Ed. 52 (2013) 13186–13200.
[2] L.F. Nazar, M. Cuisinier, Q. Pang, Lithium-sulfur batteries, MRS Bull. 39 (2014) 436–442.
[3] A. Manthiram, Y. Fu, S.H. Chung, C. Zu, Y.S. Su, Rechargeable lithium–sulfur batteries, Chem. Rev. 114 (2014) 11751–11787.
[4] Z.-S. Wu, G. Zhou, L.-C. Yin, W. Ren, F. Li, H.-M. Cheng, Graphene/metal oxide composite electrode materials for energy storage, Nano Energy 1 (2012) 107–131.
[5] X. Xu, W. Liu, Y. Kim, J. Cho, Nanostructured transition metal sulfides for lithium ion batteries: progress and challenges, Nano Today 9 (2014) 604–630.
[6] M.-S. Balogun, M. Yu, Y. Huang, C. Li, P. Fang, Y. Liu, X. Lu, Y. Tong, Binder-free Fe_2N nanoparticles on carbon textile with high power density as novel anode for high-performance flexible lithium ion batteries, Nano Energy 11 (2015) 348–355.
[7] X. Ge, Z. Li, L. Yin, Metal-organic frameworks derived porous core/shell CoP@C polyhedrons anchored on 3D reduced graphene oxide networks as anode for sodium-ion battery, Nano Energy 32 (2017) 117–124.
[8] S.-W. Kim, D.-H. Seo, H. Gwon, J. Kim, K. Kang, Fabrication of FeF_3 nanoflowers on CNT branches and their application to high power lithium rechargeable batteries, Adv. Mater. 46 (2010) 5260–5264.
[9] Y. Oumellal, A. Rougier, G.A. Nazri, J.M. Tarascon, L. Aymard, Metal hydrides for lithium-ion batteries, Nat. Mater. 7 (2008) 916–921.
[10] Y. Lu, L. Yu, X.W. Lou, Nanostructured conversion-type anode materials for advanced lithium-ion batteries, Chem 4 (2018) 972–996.
[11] Y. Oumellal, A. Rougier, J.M. Tarascon, L. Aymard, 2LiH+ M (M= Mg, Ti): new concept of negative electrode for rechargeable lithium-ion batteries, J. Power Sources 192 (2009) 698–702.
[12] W. Zaïdi, Y. Oumellal, J.P. Bonnet, J. Zhang, F. Cuevas, M. Latroche, J.L. Bobet, L. Aymard, Carboxymethylcellulose and carboxymethylcellulose-formate as binders in MgH_2–carbon composites negative electrode for lithium-ion batteries, J. Power Sources 196 (2011) 2854–2857.
[13] Y. Oumellal, W. Zaidi, J.P. Bonnet, F. Cuevas, M. Latroche, J. Zhang, J.L. Bobet, A. Rougier, L. Aymard, Reactivity of TiH_2 hydride with lithium ion: evidence for a new conversion mechanism, Int. J. Hydrog. Energy 37 (2012) 7831–7835.
[14] M. Bououdina, Y. Oumellal, L. Dupont, L. Aymard, H. Al-Gharni, A. Al-Hajry, T.A. Maark, A. De Sarkar, R. Ahuja, M.D. Deshpande, Z. Qian, A.B. Rahane, Lithium storage in amorphous TiNi hydride: electrode for rechargeable lithium-ion batteries, Mater. Chem. Phys. 141 (2013) 348–354.
[15] W. Zaïdi, J.P. Bonnet, J. Zhang, F. Cuevas, M. Latroche, S. Couillaud, J.L. Bobet, M.T. Sougrati, J.C. Jumas, L. Aymard, Reactivity of complex hydrides Mg_2FeH_6, Mg_2CoH_5 and Mg_2NiH_4 with lithium ion: far from equilibrium electrochemically driven conversion reactions, Int. J. Hydrog. Energy 38 (2013) 4798–4808.
[16] J. Zhang, W. Zaïdi, V. Paul-Boncour, K. Provost, A. Michalowicz, F. Cuevas, M. Latroche, S. Belin, J.-P. Bonnet, L. Aymard, XAS investigations on nanocrystalline Mg_2FeH_6 used as a negative electrode of Li-ion batteries, J. Mater. Chem. A 1 (2013) 4706–4717.
[17] Y. Oumellal, M. Courty, A. Rougier, G.A. Nazri, L. Aymard, Electrochemical reactivity of magnesium hydride toward lithium: new synthesis route of nano-particles suitable for hydrogen storage, Int. J. Hydrog. Energy 39 (2014) 5852–5857.
[18] Y. Oumellal, C. Zlotea, S. Bastide, C. Cachet-Vivier, E. Leonel, S. Sengmany, E. Leroy, L. Aymard, J.P. Bonnet, M. Latroche, Bottom-up preparation of MgH_2 nanoparticles with enhanced cycle life stability during electrochemical conversion in Li-ion batteries, Nanoscale 6 (2014) 14459–14466.
[19] K. Provost, J. Zhang, W. Zaïdi, V. Paul-Boncour, J.P. Bonnet, F. Cuevas, S. Belin, L. Aymard, M. Latroche, X-ray absorption spectroscopy and X-ray diffraction studies of the thermal and Li-driven electrochemical dehydrogenation of nanocrystalline complex hydrides Mg_2MH_x (M= Co, Ni), J. Phys. Chem. C 118 (2014) 29554–29567.
[20] L. Aymard, Y. Oumellal, J.P. Bonnet, Metal hydrides: an innovative and challenging conversion reaction anode for lithium-ion batteries, Beilstein J. Nanotechnol. 6 (2015) 1821–1839.
[21] L. Huang, L. Aymard, J.P. Bonnet, MgH_2–TiH_2 mixture as an anode for lithium-ion batteries: synergic enhancement of the conversion electrode electrochemical performance, J. Mater. Chem. A 3 (2015) 15091–15096.
[22] L. Silvestri, S. Forgia, L. Farina, D. Meggiolaro, S. Panero, A. La Barbera, S. Brutti, P. Reale, Lithium alanates as negative electrodes in lithium-ion batteries, ChemElectroChem 2 (2015) 877–886.
[23] J.A. Teprovich, J. Zhang, H. Colón-Mercado, F. Cuevas, B. Peters, S. Greenway, R. Zidan, M. Latroche, Li-driven electrochemical conversion reaction of AlH_3, $LiAlH_4$, and $NaAlH_4$, J. Phys. Chem. C 119 (2015) 4666–4674.
[24] L. Silvestri, L. Farina, D. Meggiolaro, S. Panero, F. Padella, S. Brutti, P. Reale, Reactivity of sodium alanates in lithium batteries, J. Phys. Chem. C 119 (2015) 28766–28775.
[25] L. Cirrincione, L. Silvestri, C. Mallia, P.E. Stallworth, S. Greenbaum, S. Brutti, S. Panero, P. Reale, Investigation of the effects of mechanochemical treatment on $NaAlH_4$ based anode materials for Li-ion batteries, J. Electrochem. Soc. 163 (2016) A2628–A2635.
[26] L. Silvestri, A. Paolone, L. Cirrincione, P. Stallworth, S. Greenbaum, S. Panero, S. Brutti, P. Reale, $NaAlH_4$ nanoconfinement in a mesoporous carbon for application in lithium ion batteries, J. Electrochem. Soc. 164 (2017) A1120–A1125.
[27] P. Huen, F. Peru, G. Charalambopoulou, T.A. Steriotis, T.R. Jensen, D.B. Ravnsbæk, Nanoconfined $NaAlH_4$ conversion electrodes for Li batteries, ACS Omega 2 (2017) 1956–1967.
[28] F. Wu, Z. Chen, B. Lei, J. Wang, K. Xie, Y. Song, D. Sun, F. Fang, Improved reversibility and cyclic stability of $NaAlH_4$ anode for lithium ion batteries, Electrochim. Acta 257 (2017) 321–327.
[29] L. Silvestri, M.A. Navarra, S. Brutti, P. Reale, Failure mechanism of $NaAlH_4$ negative electrodes in lithium cells, Electrochim. Acta 253 (2017) 218–226.
[30] J.E. Fonneløp, O.M. Løvvik, M.H. Sørby, H.W. Brinks, B.C. Hauback, Adjustment of the decomposition path for Na_2LiAlH_6 by TiF_3 addition, Int. J. Hydrog. Energy 36 (2011) 12279–12285.
[31] H. Liu, X. Wang, Z. Dong, G. Cao, Y. Liu, L. Chen, M. Yan, Dehydriding properties of γ-AlH_3, Int. J. Hydrog. Energy 38 (2013) 10851–10856.
[32] C. Weidenthaler, A. Pommerin, M. Felderhoff, B. Bogdanović, F. Schüth, Evidence for the existence of β-Na_3AlH_6: monitoring the phase transformation from α-Na_3AlH_6 by in situ methods, J. Alloy. Compd. 398 (2005) 228–234 (398).
[33] R. Zidan, B.L. Garcia-Diaz, C.S. Fewox, A.C. Stowe, J.R. Gray, A.G. Harter, Aluminium hydride: a reversible material for hydrogen storage, Chem. Commun. 25 (2009) 3717–3719.
[34] L. Zeng, T. Ichikawa, K. Kawahito, H. Miyaoka, Y. Kojima, Bulk-type all-solid-state lithium-ion batteries: remarkable performances of a carbon nanofiber-supported MgH_2 composite electrode, ACS Appl. Mater. Interfaces 9 (2017) 2261–2266.
[35] N. Ohta, K. Takada, L. Zhang, R. Ma, M. Osada, T. Sasaki, Enhancement of the high rate capability of solid-state lithium batteries by nanoscale interfacial modification, Adv. Mater. 18 (2006) 2226–2229.
[36] A. El kharbachi, H.F. Andersen, M.H. Sørby, P.E. Vullum, J.P. Mæhlen, B.C. Hauback, Morphology effects in MgH_2 anode for lithium ion batteries, Int. J. Hydrog. Energy 42 (2017) 22551–22556.
[37] L. Zeng, K. Kawahito, S. Ikeda, T. Ichikawa, H. Miyaoka, Y. Kojima, Metal hydride-based materials towards high performance negative electrodes for all-solid-state lithium-ion batteries, Chem. Commun. 51 (2015) 9773–9776.
[38] P. López-Aranguren, N. Berti, A.H. Dao, J.X. Zhang, F. Cuevas, M. Latroche, C. Jordy, An all-solid-state metal hydride–Sulfur lithium-ion battery, J. Power Sources 357 (2017) 56–60.